Article citation info:
Kumar MA, Ramesh P, Gunasekaran EJ, Karthikeyan M. Synergy between start of fuel injection and injector guidance for precision combustion in GDI engines using CFD tools. Combustion Engines. 0000;XXX(X):xx-xx. https://doi.org/10.19206/CE-225507

Madireddy Ananda KUMAR
Perumal RAMESH
Edward James GUNASEKARAN
Mahendiran KARTHIKEYAN

Combustion Engines
Polish Scientific Society of Combustion Engines

Synergy between the start of fuel injection and injector guidance for precision combustion in GDI engines using CFD tools

ARTICLE INFO

Received: 14 October 2025
Revised: 17 March 2026
Accepted: 6 July 2026
Available online: 12 September 2026

Combustion behaviour in gasoline direct injection engines is strongly influenced by the interaction between start of injection timing and injector spray guidance, because these parameters jointly control spray–air interaction, mixture stratification, ignition stability, combustion phasing, and pollutant formation. This study applies three-dimensional moving-mesh computational fluid dynamics to evaluate the coupled effects of injection timing and injector guidance in a single-cylinder, four-stroke, gasoline direct injection engine with a 86 mm bore, 86 mm stroke, a compression ratio of 9.2, and an engine speed of 1000 rpm. Three injection timings were examined relative to intake-valve operation: after intake valve opening, at maximum intake valve lift, and after intake valve closing. For each timing, air-guided, wall-guided, and spray-guided injector orientations were assessed under identical operating conditions. The spray process was represented using detailed breakup, evaporation, and wall-interaction sub-models at an injection pressure of 50 bar, with 4.398 × 10^{-5} kg of fuel injected per cycle and 300,000 computational parcels. Combustion was simulated using the SAGE detailed-chemistry solver, while nitrogen oxide formation was represented using the extended Zeldovich mechanism. The results show that injection at maximum intake valve lift provides the most favourable interaction between spray momentum and intake-driven turbulence, improving mixture preparation and producing compact heat release. Among the investigated cases, wall-guided injection at maximum intake valve lift delivered the strongest pressure and temperature development, the sharpest heat-release profile, the lowest carbon monoxide and unburned hydrocarbon levels, and the highest carbon dioxide formation, indicating more complete oxidation. Late injection after intake valve closing produced poor mixture preparation, weak heat release, and increased incomplete-combustion products, particularly for the spray-guided case. The study demonstrates that injection timing and injector guidance must be optimised jointly rather than independently to achieve precision combustion with improved efficiency and controlled emissions in modern gasoline direct injection engines.

Key words: *emissions gasoline direct injection, start of injection, injector guidance, mixture formation, spray–flow interaction; CFD, heat release, emissions*

1. Introduction

Internal combustion engines (ICEs) remain essential in transportation and distributed power because of high specific energy density fuels, mature infrastructure, and robust cold-start performance [14–16]. However, continued reliance on fossil fuels accelerates resource depletion [20, 25], and combustion-derived pollutants remain a dominant contributor to air-quality degradation. In parallel, noise and vibration continue to motivate efficiency-focused design improvements that reduce overall fuel consumption and, by extension, fleet-level emissions [13, 22]. These constraints have intensified the development of combustion concepts that provide high efficiency without compromising regulatory compliance.

Gasoline direct injection (GDI) has become a key technology for modern spark-ignition powertrains because it enables direct control of in-cylinder mixture preparation through high-pressure fuel delivery, thereby supporting both homogeneous and stratified operating modes [1, 2, 12, 27]. Relative to port fuel injection (PFI), GDI can improve knock resistance through in-cylinder evaporative cooling, enable higher compression ratios, and enhance transient response through cycle-resolved fuel metering [3, 4]. At part load, throttle-based premixing in conventional gasoline engines introduces pumping losses, whereas direct injection improves flexibility in air–fuel management and reduces intake-port wall film formation, improving cycle-to-cycle consistency and response to rapid load changes [4, 18, 19].

Mixture preparation in GDI engines is typically classified into homogeneous and stratified regimes, which are realised through different spray targeting philosophies: wall-guided, spray-guided, air-guided, and hybrid approaches [7]. Wall-guided concepts intentionally exploit piston crown geometry to redirect spray momentum, spray-guided strategies rely on injector–spark plug alignment and nozzle targeting, and air-guided concepts use intake-generated tumble and swirl to transport vapour toward the ignition region. Although wall-guided injection is historically well established, it remains practically relevant because modern chamber design, injector hardware, and calibration strategies have shifted the trade space: the same guidance concept can yield materially different outcomes when combined with contemporary valve events, strong intake tumble management, and optimised SOI scheduling. Importantly, guidance strategy and SOI timing interact nonlinearly, because SOI controls both the residence time for evaporation/mixing and the intensity of the flow structures that entrain the spray, while guidance determines where the spray momentum is deposited and how robustly the ignition region is enriched [17, 21, 26].

Recent gasoline direct injection research has increasingly focused on injection timing, injector-hole geometry, spray targeting, injection-rate shaping, injector-zone particulate formation, and alternative oxygenated fuels. Recent studies on direct-injection spark-ignition operation using n-butanol and bio-butanol show that injection timing strongly affects mixture homogeneity, combustion quality, and trends in carbon monoxide, hydrocarbons, soot, and nitrogen oxides [6, 8, 9, 11]. Similarly, recent computational work on spray-guided GDI combustion has shown that injector type and intake boosting can significantly affect combustion and emissions, while recent injector-zone modelling studies identify local liquid films and rich zones as important sources of particulate-related emissions in GDI engines [10, 23, 24]. However, many of these studies examine injection timing, injector design, fuel effects, or spray guidance individually, whereas fewer studies systematically quantify how injection timing and injector guidance interact under the same engine geometry, fuel delivery, combustion model, and boundary conditions.

The present study addresses this gap by conducting a controlled three-by-three factorial CFD investigation of three start-of-injection timings and three injector guidance strategies in a single GDI engine configuration. The contribution is not the isolated evaluation of wall-guided, air-guided, or spray-guided injection, but the identification of how each guidance strategy is strengthened or weakened by the valve-event-dependent in-cylinder flow field. The study therefore provides three specific contributions to the state of the art: first, it quantifies how injection timing relative to intake-valve motion changes tumble, swirl, mixture stratification, and liquid-fuel persistence; second, it explains why wall-guided injection remains relevant when piston-crown redirection is synchronised with maximum intake-induced turbulence; and third, it identifies the combustion–emission trade-off that results when compact heat release reduces incomplete-combustion products but increases sensitivity to thermal nitrogen oxide formation. This coupling-focused analysis provides calibration-relevant guidance for precision combustion development in modern and future GDI engines, including engines operating with gasoline-range surrogate, oxygenated, or synthetic fuels.

2. Methodology

2.1. Engine geometry and initialization

The computational model represents a single-cylinder, four-stroke GDI engine with Siamese intake ports. The geometry was created in CAE software and imported in STL format to preserve the piston crown, valve seats, and cylinder head contours. The cylinder head employs a domed combustion chamber with a centrally located spark plug to support symmetric ignition kernel development in the present configuration. The bore and stroke were each set to 86 mm, the connecting rod length to 145 mm, and the geometric compression ratio to 9.2:1. The engine speed was fixed at 1000 rpm.

The bore and stroke dimensions were set to 86 mm each, resulting in a square configuration. The connecting rod length was set to 145 mm, and the geometric compression ratio was fixed at 9.2:1. The piston featured a shallow bowl with offset curvature, optimized to assist charge tumble and spray interaction. A centrally located spark plug was incorporated to provide symmetrical ignition kernel growth, a critical factor in GDI combustion. Figures 1–3 illustrate the top view, front view, and isometric projections of the engine chamber geometry, respectively.

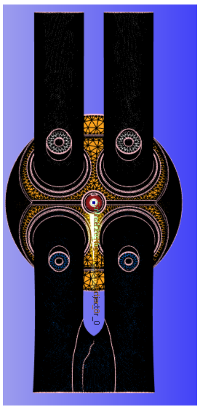

Fig. 1. Top view of Siamese port GDI engine geometry

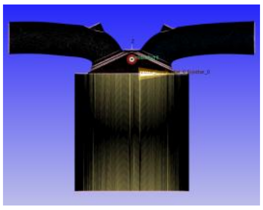

Fig. 2. Front view of the Siamese port GDI engine geometry

Fig. 3. Pictorial view of Siamese port GDI engine geometry

Table 1 summarizes the main engine specifications. The valve lift profiles, shown in Tables 2–3, were modelled according to literature values. The intake valve opened at −370°CA and closed at −125°CA, while the exhaust valve opened at 125°CA and closed at 370°CA. The minimum valve lift was maintained at 0.0002 m, ensuring computational stability and realistic gas exchange.

Table 1. Specific engine configuration

Parameter	Value	Unit
Cylinder bore	86	mm
Stroke (2 × crank radius)	86	mm
Connecting rod length	145	mm
Crank speed	1000	rpm

Table 2. Valve lift profile configuration

Parameter	Intake valve	Exhaust valve
Type	cyclic	cyclic
Period	720.0	720.0
Direction (x, y, z)	–0.421848, 0.0, 0.906667	0.421848, 0.0, 0.906667
Minimum Lift (m)	0.0002	0.0002

Table 3. Valve lift profile position of crank angle

Lift position (mm)	Crank angle position [°CA]	
	Intake valve	Exhaust valve
0.0	–370.0	126
3.8×10^{-5}	–369.0	127
7.6×10^{-5}	–368.0	128
0.000114	–367.0	129
0.000152	–366.0	130
0.00019	–365.0	131

The computational mesh was generated using a hybrid polyhedral–tetrahedral scheme. Refinement zones were applied around the injector nozzle, the spark plug, and the piston bowl to adequately capture spray–wall interactions and flame front development. A moving-mesh (Arbitrary Lagrangian–Eulerian) method was implemented to model piston motion, maintaining consistent cell quality throughout the full engine cycle. At intake valve closure (IVC), the mesh was initialized with uniform thermodynamic conditions: pressure = 1 atm, temperature = 298 K, velocity = 0 m/s, turbulent kinetic energy k = 1.0 m²/s², and turbulent dissipation rate ε = 164 m²/s³.

The in-cylinder gas composition was initialized with mass fractions: O_2 = 0.03, N_2 = 0.73, CO_2 = 0.15, and H_2O = 0.09, corresponding to typical stoichiometric exhaust gas recirculation conditions. The intake port region was maintained at 303 K, while the exhaust manifold was initialized with a matching composition to preserve transient gas dynamics.

The compression ratio was calculated using:

$$CR = (V_d + V_c)/V_c$$

where: V_d is the displacement volume and V_c is the clearance volume. With the given bore, stroke, and compression ratio, the clearance volume was determined to be consistent with experimental references in the literature [11].

This initialization strategy ensured that the model accurately reproduced realistic thermodynamic states for subsequent spray and combustion simulations.

2.2. Fuel injection and spray modelling

Fuel injection was modelled as a high-pressure direct injection event with an injection pressure of 50 bar. Each injection delivered a mass of 4.398×10^{-5} kg of gasoline per cycle, represented by 300,000 discrete parcels in the Lagrangian framework. The blob injection model was employed, wherein the initial droplet size corresponded to the nozzle exit diameter.

Table 4. Events of region period in cyclic for 720-degree crank angle

S.no	Event	Region A	Region B	Start of crank angle [deg]
1	Open	Cylinder	Intake system	–370
2	Close	Cylinder	Intake system	–125
3	Open	Cylinder	Exhaust system	125
4	Close	Cylinder	Exhaust system	370

Injection strategies were simulated for three distinct timings relative to the intake valve operation:

aIVO – injection after intake valve opening,

mIVL – injection at maximum intake valve lift, and

aIVC – injection after intake valve closure.

These timings capture the transition from early homogeneous-charge operation to late stratified-charge operation.

Spray breakup and atomization were modelled using the Kelvin-Helmholtz (KH) and Rayleigh-Taylor (RT) secondary breakup models. The governing equation for droplet stripping under KH instability is:

$$\frac{dD}{dt} = -\frac{2\Lambda}{3}\frac{\rho_g}{\rho_l}\frac{U_r}{D}$$

where D is the droplet diameter, Λ is the KH wavelength, ρ_g and ρ_l are the gas and liquid densities, and U_r is the relative velocity between droplet and surrounding gas.

The RT breakup was applied when the pressure differential across the droplet surface exceeded the stabilizing surface tension force, expressed as:

$$a = \frac{\Delta P}{\rho_l \cdot D}$$

where: a is droplet acceleration due to instability and ΔP is the pressure difference. The KH constants were defined as: size = 0.61, velocity = 0.188, breakup time = 7.0. RT constants included: size = 0.6, time = 1.0, and length = 0. A mass fraction of 5% was transferred from parent to child droplets during each breakup event.

Droplet evaporation was governed by the Frössling correlation:

$$\frac{dm}{dt} = -\pi D Sh \cdot D_{AB} \cdot \rho_g \ln(1 + B_M)$$

where: Sh is the Sherwood number, D_{AB} is the mass diffusivity, and B_M is the Spalding mass transfer number.

This comprehensive spray model captured atomization, evaporation, and wall interaction effects essential for GDI combustion analysis.

2.3. Combustion and emission modelling

Combustion was simulated using the SAGE detailed-chemistry framework, which integrates finite-rate chemical source terms into the resolved flow field to predict heat release and the evolution of intermediate species. Iso-octane (IC_8H_{18}) was adopted as the gasoline surrogate fuel, consistent with the fuel specification in Table 5. In SAGE, the net production rate of species iii is computed from the sum of elementary reactions, expressed generically as:

$$\frac{dY_i}{dt} = \frac{1}{\rho}\sum_{r=1}^{N_r} \nu_{i,r} \cdot \omega_r$$

where: Y_i is the mass fraction of species i, $\nu_{i,r}$ is the stoichiometric coefficient of species i in reaction r, and ω_r is the net reaction rate given by the Arrhenius law:

$$\omega_r = A \cdot T^n \cdot \exp\left(-\frac{E_a}{RT}\right)\prod_j C_j^{\nu_{j,r}}$$

with A as the pre-exponential factor, n the temperature exponent, E_a the activation energy, and C_j the molar concentration of reactant j.

Thermal NO formation was modelled using the extended Zeldovich pathway (Table 5), and CO/UHC were resolved using the enabled emissions sub-models consistent with the solver configuration.

2.4. Governing framework

The governing equations for conservation of mass, momentum, species transport, and energy were solved in conjunction with Reynolds-Averaged Navier-Stokes (RANS) turbulence closure. The standard *k–ε* model was selected, offering computational robustness while capturing turbulence-driven mixing. The transport equations are expressed as:

$$\frac{\partial(\rho k)}{\partial t} + \nabla \cdot (\rho k \mathbf{u}) = \nabla \cdot \left[\left(\mu + \frac{\mu_t}{\sigma_k}\right)\nabla k\right] + P_k - \rho\epsilon$$

$$\frac{\partial(\rho\epsilon)}{\partial t} + \nabla \cdot (\rho\epsilon\mathbf{u}) = \nabla \cdot \left[\left(\mu + \frac{\mu_t}{\sigma_\epsilon}\right)\nabla\varepsilon\right] + C_{1\epsilon}\frac{\epsilon}{k}P_k - C_{2\epsilon}\rho\frac{\epsilon^2}{k}$$

where: k is the turbulent kinetic energy, ϵ is the dissipation rate, μ_t is the turbulent viscosity, and P_k is the turbulence production term.

Heat transfer at solid boundaries was modelled using the O'Rourke and Amsden wall function approach, where the base distance to the wall was set equal to the full computational cell size. This ensured stable treatment of wall heat flux in the near-wall region.

Flame front propagation was represented by iso-surfaces of progress variable, with the turbulent flame speed S_T controlling the advancement of the front:

$$S_T = S_L + u'$$

where: S_L is the laminar flame speed and u′ is the turbulent velocity fluctuation derived from RANS.

2.5. Combustion model settings

The combustion and emissions settings applied in SAGE are summarised in Table 5, including the combustion temperature cut-off (600.0 K), minimum hydrocarbon mole fraction (1×10^{-10}), adaptive zoning (2D) with temperature bin size (5.0 K) and reaction ratio bin size (0.05), and CVODES dense-solver tolerances (relative 0.0001; absolute 1×10^{-14}).

Table 5. Combustion modeling settings (SAGE)

Setting parameter	Value
Fuel species name	IC_8H_{18}
Temporal type	SEQUENTIAL
Combustion temperature cut-off	600.0 K
Minimum HC species mole fraction	1×10^{-10}
Surface/emissions model	Surface chemistry and emissions model enabled
Use adaptive zoning	Enabled
Dimension of adaptive zoning	2
Temperature bin size	5.0 K
Reaction ratio bin size	0.05
Generate adaptive zoning output	Enabled
Use heat release mapping	Enabled
Re-solve Option	Only re-solve if the temperature changes by specified value
Re-solve temperature	2.0 K
Use analytical Jacobian	Enabled
Relative tolerance	0.0001
Absolute tolerance	1×10^{-14}
Solver	CVODES with dense solver
Combustion region	Cylinder
Temporal type (region)	CYCLIC
Cycle period (region)	720 deg
Start time (region)	–21 deg
End time (region)	150 deg
Thermal NOx model	Extended Zeldovich (enabled)
Equivalence ratio	1.2
Mass scaling factor (NO to NO_x)	1.533

The combustion window was restricted to −21°CA to 150°CA to represent the physically relevant ignition-to-burn interval under the present operating condition, while the full cycle was simulated as described in Section 2.7. Thermal NO formation was enabled through the extended Zeldovich model with a mass scaling factor (NO to NO_x) of 1.533 and the global equivalence ratio set to ϕ=1.2/phi = 1.2ϕ = 1.2 (Table 5).

2.6. Spark-ignition settings

Ignition was represented using a dual-energy source model. Two spherical ignition kernels were initialized near the centrally located spark plug. Both sources supplied an energy of 0.02 J, with a maximum allowable kernel temperature of 5000 K to avoid nonphysical energy spikes.

Source 1: active between −20° and −19.5°CA

Source 2: active between −20° and −10°CA

This dual-source configuration ensured stable ignition and consistent flame kernel growth. The cyclic period of 720°CA was maintained, with ignition preceding top dead center (TDC) to allow adequate flame propagation during the compression stroke.

2.7. Solver configuration

The simulation cycle extended from −380° to +360°CA, covering intake, compression, power, and exhaust events. Combustion was restricted to the period between −21°CA and 150°CA, reflecting the physical ignition-to-burn duration. A variable time-step algorithm was employed to ensure convergence while resolving transient chemical kinetics.

Initial time step: 1×10^{-6} s

Minimum time step: 1×10^{-7} s

Maximum time step: 1×10^{-4} s

The Courant-Friedrichs-Lewy (CFL) condition was enforced with convection = 1.0, diffusion = 2.0, and Mach number = 50, ensuring numerical stability. Sub-cycling parameters were applied to refine discrete physical processes: droplet motion = 1.5, chemical reaction = 0.5, collision grid = 1.0, and moving boundaries = 0.5.

2.8. Pollutant formation models

Pollutant emissions were resolved through detailed sub-models:

1. Carbon Monoxide (CO) – predicted via a three-step global mechanism, accounting for incomplete oxidation of hydrocarbons.
2. Unburned Hydrocarbons (UHC) – modelled through crevice and wall-quenching sub-processes.
3. Nitric Oxide (NO) – calculated using the Extended Zeldovich mechanism, incorporating thermal, prompt, and N_2O intermediate pathways:

$$O + N_2 \rightarrow NO + N$$

$$N + O_2 \rightarrow NO + O$$

$$N + OH \rightarrow NO + H$$

Soot modelling was not activated in the present study to maintain consistency with the selected emissions sub-model set and to focus the analysis on SOI–guidance coupling effects on mixture preparation, heat release, CO, UHC, and thermal NO_x formation under the specified global equivalence ratio (ϕ=1.2/phi = 1.2ϕ = 1.2).

The selected modelling framework balances computational cost and accuracy by coupling RANS turbulence closure with detailed chemistry. Adaptive zoning reduces stiffness in chemical integration by dynamically refining the spatial–temporal resolution in high-gradient regions. The dual-energy spark strategy prevents misfire while controlling maximum kernel temperatures.

The simulation setup therefore captures both laminar flame development and turbulence-enhanced propagation, which are essential for reproducing real GDI combustion. Furthermore, the inclusion of global, detailed submodels for CO, UHC, and NO provides robust predictions of regulated emissions, directly supporting comparisons with experimental data.

2.9. Validation

Validation of the computational model was undertaken by benchmarking in-cylinder flow predictions against experimental data from the literature [2]. The focus of the comparison was on the axial distribution of fluctuation velocity within the cylinder, which provides a sensitive measure of turbulence characteristics and numerical accuracy. In addition, a grid independence study was performed using three discretization levels with characteristic grid sizes of 4 mm, 6 mm, and 8 mm (Fig. 4).

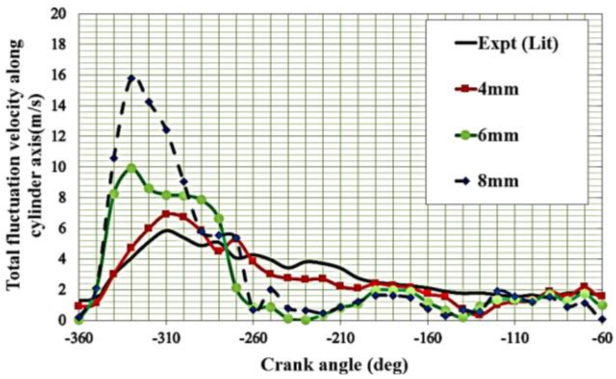

Fig. 4. Grid size study with experimental data available in literature [27]

2.10. Grid independence analysis

The simulation results reproduced the characteristic trend of fluctuation velocity, with the highest values occurring near −310° crank angle (DCA) across all meshes. The 8 mm grid predicted larger velocity magnitudes, reflecting the inability of a coarse mesh to resolve finer-scale turbulent fluctuations. In contrast, the 4 mm mesh provided the closest agreement with the experimental dataset, accurately reproducing both the amplitude and location of the velocity peak.

To assess grid sensitivity quantitatively, the grid convergence index (GCI) and relative error norms were computed. The percentage deviation between numerical and experimental values was determined using the following expression:

$$\%\mathrm{Error} = \frac{\left|\mathrm{U_{CFD}} - \mathrm{U_{exp}}\right|}{\mathrm{U_{exp}}} \times 100$$

where U_{CFD} represents the predicted fluctuation velocity and U_{exp} denotes the corresponding experimental value. The $L_{2\text{-norm}}$ of the error was additionally calculated as:

$$\mathrm{L_2} = \sqrt{\frac{1}{\mathrm{N}}\sum_{\mathrm{i}=1}^{\mathrm{N}}\left(\mathrm{U_{CFD,i}} - \mathrm{U_{exp,i}}\right)^2}$$

with N representing the total number of data points considered along the crank angle range.

Application of these metrics revealed that the 4 mm mesh consistently exhibited an error margin below 5%, whereas the 6 mm and 8 mm grids showed larger deviations, particularly near the velocity peak. This confirms that the finer discretization enhances the capture of turbulent flow structures, thereby improving model fidelity.

2.11. Flow evolution across crank angles

For validation, the simulation was performed without combustion or fuel injection to isolate the influence of fluid dynamics. The flow field was monitored from −360° to −60°CA, corresponding to the compression stroke prior to ignition. Across all grid sizes, fluctuation velocity declined progressively as the piston approached top dead center, with a marked decrease beyond −60°CA. This behavior aligns with the expected damping of turbulence as the available cylinder volume decreases during compression.

The 4 mm grid not only reproduced the trend but also captured the exact decay rate of the velocity fluctuations, closely matching the experimental trajectory. This highlights the importance of adequate spatial resolution for predicting turbulence dissipation and verifying the temporal evolution during the compression phase.

2.12. Selection of optimal grid and implications for CFD framework

While finer grids inevitably increase computational cost, the grid independence study establishes that the 4 mm mesh provides the optimal balance between accuracy and efficiency. Its close correspondence with experimental measurements validates its use for all subsequent simulations of mixture preparation, flame propagation, and emissions modeling.

The successful validation against experimental benchmarks and the demonstration of grid independence confirm the robustness of the present CFD framework. By accurately capturing the fluctuation velocity field, the model ensures a reliable foundation for investigating injection timing, spray guidance, and combustion strategies. The fidelity of the baseline hydrodynamic model is critical for subsequent predictive simulations of turbulent flame development, pollutant formation, and combustion efficiency.

3. Results and discussion

3.1. Overview of case matrix

The comparative study evaluates nine injection configurations distinguished by guidance mode – Air-Guided Injection (AG-I), Wall-Guided Injection (WG-I), and Spray-Guided Injection (SG-I) and by start-of-injection (SOI) timing, namely after Inlet Valve Opening (aIVO), at Maximum Inlet Valve Lift (mIVL), and after Inlet Valve Closing (aIVC). This full-factorial combination yields a 3-by-3 case matrix. All simulations were performed under identical boundary conditions, with a constant injection pressure of

50 bar, a total injected fuel mass of 4.398×10^{-5} kg, and approximately 300,000 parcels in the discrete spray model. The global equivalence ratio was maintained at $\phi = 1.2$, the spark discharge energy was fixed at 0.02 J per source, and the ignition timing was held at 20°CA bTDC. This consistent baseline isolates the coupled influence of injector guidance and SOI on in-cylinder mixture preparation, combustion phasing, and emissions.

3.2. Fluid motion characteristics: tumble and swirl

Figures 5–7 illustrate the evolution of tumble ratios about the X and Y axes, together with swirl ratio about the cylinder axis, for the nine strategies. Tumble ratios characterize vertical and lateral recirculation, while swirl ratio quantifies circumferential rotation. These motions enhance turbulence intensity and, by extension, mixing and flame wrinkling.

The simulations reveal that mIVL timing produces the strongest tumble and swirl for all guidance strategies. This outcome is consistent with the physical state of the cylinder: valve lift is maximized, airflow momentum peaks, and the entrained spray is embedded in a highly energetic vortex field. WG-I@mIVL produces particularly pronounced tumble, benefiting from geometric steering of the jet onto the piston crown, which transforms impingement into sheet-like ligaments. AG-I@mIVL also demonstrates robust tumble, although its reliance on bulk airflow rather than solid-surface reflection renders it more sensitive to instantaneous vortex orientation. By contrast, SG-I@mIVL produces weaker secondary flows because the plume penetrates centrally with limited interaction with the piston and wall surfaces.

Early injections (aIVO) display moderate tumble and swirl. Although airflow is present, the valve lift is not yet maximal, and turbulence structures are still developing. Late injections (aIVC) coincide with the collapse of intake-driven motion; hence, tumble and swirl ratios are markedly reduced. In these cases, plume-driven momentum dominates, resulting in poorer entrainment of spray droplets.

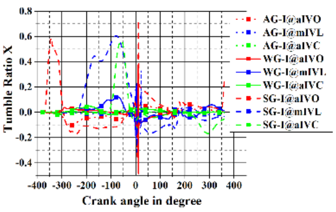

Fig. 5. Fluid flow tumble ratio about the x-axis in various guidance of injection

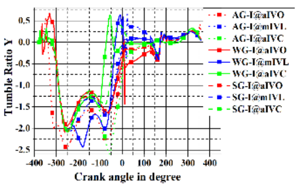

Fig. 6. Fluid flow tumble ratio about the y-axis in various guidance of injection

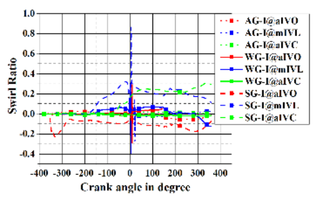

Fig. 7. Fluid flow swirl ratio in various guidance of injection

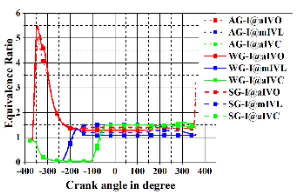

Fig. 8. Temporal variation of equivalence ratio

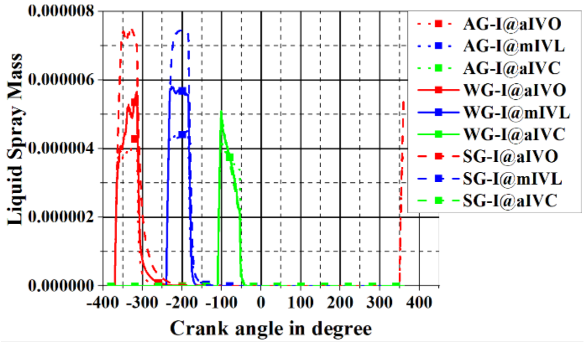

Fig. 9. Temporal variation of fuel spray mass in liquid

3.3. Equivalence ratio evolution

The temporal variation of equivalence ratio, shown in Fig. 8, reflects the overall mixing of fuel vapor with air across the engine cycle. Uniformity of equivalence ratio distribution is crucial for ignition stability and for limiting pollutant formation.

At aIVO, the equivalence ratio fluctuates over an extended premixing interval, with mixtures gradually homogenizing by the time of spark at −20°CA. However, local wall interactions introduce zones of lean and rich bias, especially in spray-guided cases where vapor clouds remain concentrated near the jet axis. At mIVL, equivalence ratio distributions are notably more uniform. WG-I@mIVL achieves near-stoichiometric conditions in the ignition region, supported by piston-crown redirection and strong tumble entrainment. AG-I@mIVL also delivers consistent mixtures but is somewhat more cycle-sensitive. SG-I @mIVL, while improved relative to aIVO, retains slightly higher spatial variance, producing localized rich kernels near the spark.

The aIVC injections exhibit the least favorable evolution of the equivalence ratio. The short residence time on the order of 17.5 ms at 1000 rpm restricts mixing, and the decay of turbulence further hampers distribution. Rich vapor zones persist near the injection site, while lean regions occur elsewhere, increasing the risk of misfire and incomplete combustion.

3.4. Liquid spray mass

The evolution of liquid-phase spray mass is presented in Fig. 9. For aIVO cases, liquid mass appears earliest and persists over a long crank-angle duration, consistent with the long premixing window of ~58.3 ms before spark. Over time, evaporation reduces the mass, though residual wall films may remain. mIVL injections show mid-length persistence, typically ~35 ms before spark, with efficient atomization and evaporation. The liquid mass curve for WG-I @mIVL decays more rapidly than for AG-I@mIVL or SG-I @mIVL, confirming that wall interactions enhance sheet breakup and droplet surface area.

By contrast, aIVC injections exhibit the shortest persistence. The injection occurs only ~17.5 ms before spark, so the liquid spray is visible late in the cycle, with limited time for vaporization. While peak liquid mass is lower, localized stratification is higher because droplets and vapor remain concentrated near the jet axis. SG-I@aIVC retains liquid near the ignition timing, a source of instability and poor repeatability.

3.5. Temporal fuel–air mixture formation

Tables 6–8 provide contour snapshots of the equivalence ratio distribution for the three SOI timings across all guidance modes. Red regions correspond to fuel-rich zones, while blue regions indicate lean mixtures.

For aIVO (Table 6), early stratification dominates, with Air- and Wall-Guided injections producing moderately rich cores that disperse gradually. Turbulence and valve-induced flows assist in transport, but mixture uniformity near ignition remains incomplete. In mIVL cases (Table 7), mixture quality improves significantly. WG-I@mIVL shows a centrally stratified, well-mixed mixture near the spark plug, ideal for stable ignition under slightly lean or stoichiometric conditions. SG-I@mIVL, however, creates locally rich patches, visible as persistent red regions, which may affect the consistency of flame propagation.

Table 6. Temporal fuel mixture at SOI after inlet valve opening

Crank angle [°CA]	Air guide fuel injection	Wall guide fuel injection	Spray guide fuel injection	Direction and color indices
–367	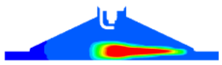			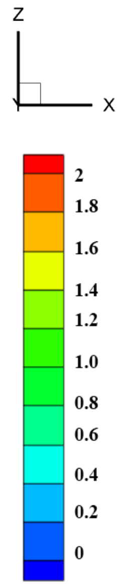
–337				
–307	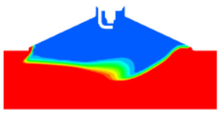	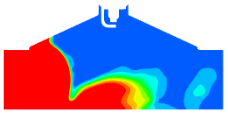	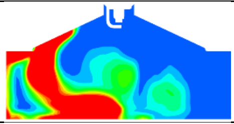	
–277	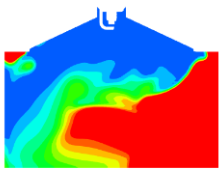	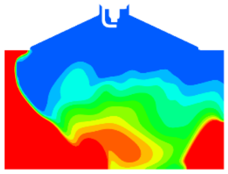	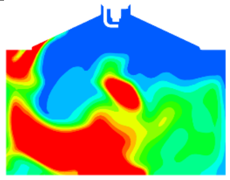	
–247	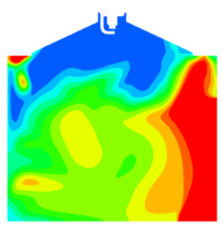	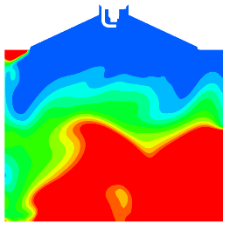	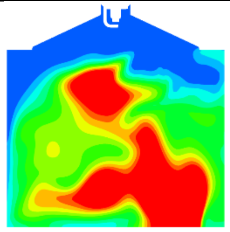	
–125		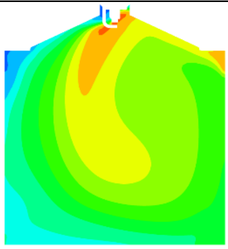		
–30		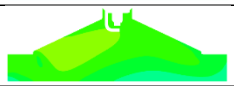	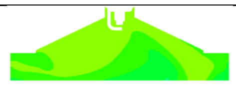	
–20				
–10	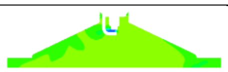	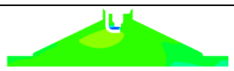	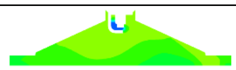	
–6	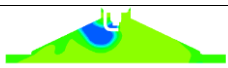		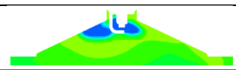	
0	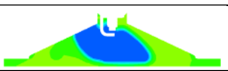	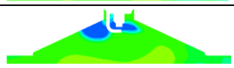	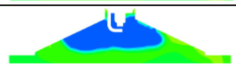	
6		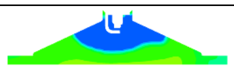	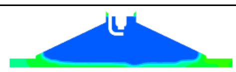	
10		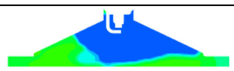		

Table 7. Temporal fuel mixture at SOI maximum intake valve lift

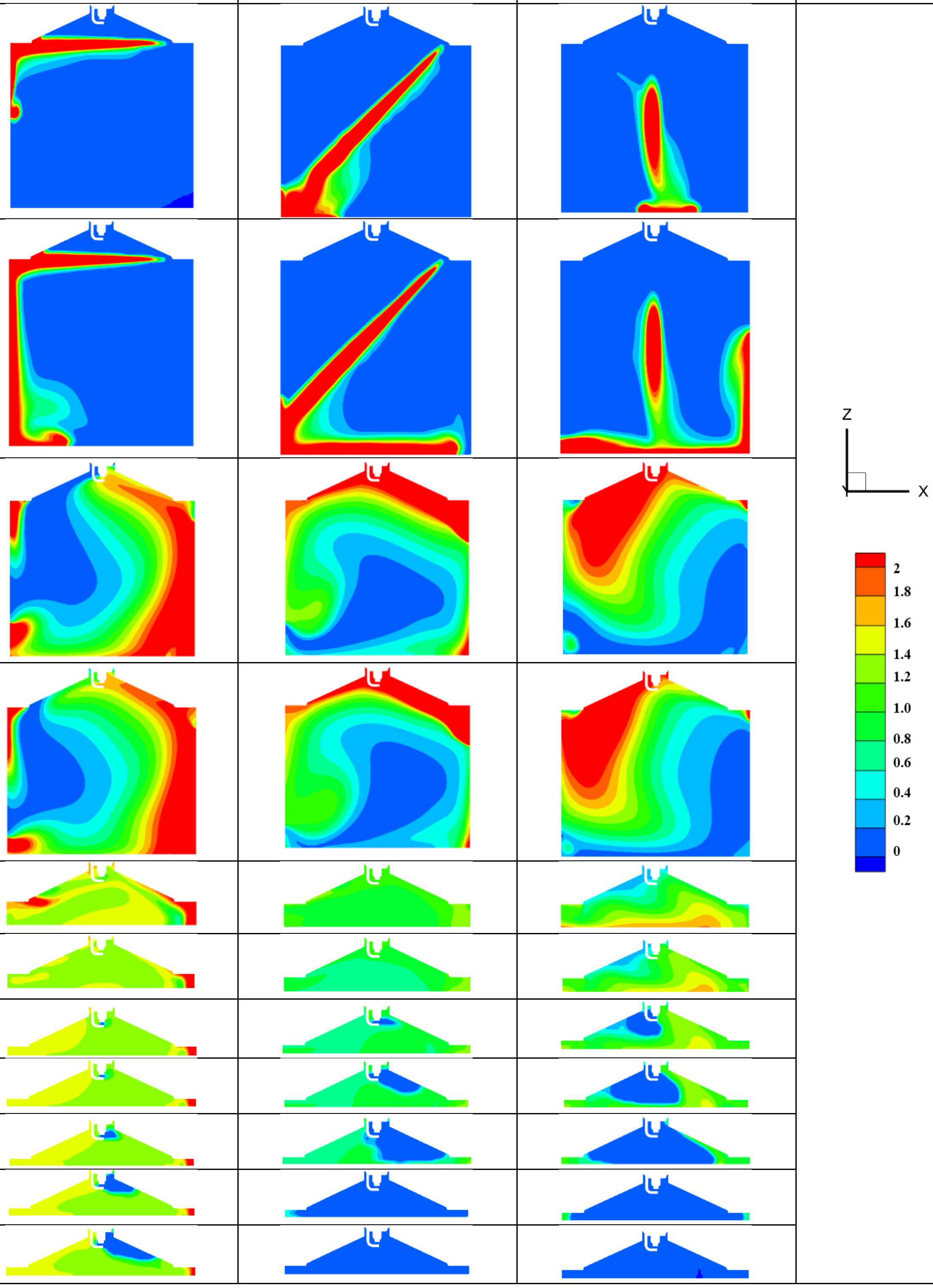

Crank angle [°CA]	Air guide fuel injection	Wall guide fuel injection	Spray guide fuel injection	Direction and color indices
–230				
–200				
–120				
–110				
–30				
–20				
–10				
–5				
0				
5				
10				

Late injection aIVC (Table 8) leads to poor mixing across all strategies. Fuel-rich pockets remain highly localized, particularly in SG-I@aIVC, where vapor accumulates near the spark. Air-Guided injection fares slightly better by distributing vapor through residual airflow, but overall mixture quality is degraded compared to aIVO and mIVL.

Colour scale: equivalence ratio, ϕ (–); red indicates fuel-rich regions, blue indicates lean regions. Colour scale: temperature, T (K).

Table 8. Temporal fuel mixture at SOI after intake valve closing

Crank angle [°CA]	Air guide fuel injection	Wall guide fuel injection	Spray guide fuel injection	Direction and color indices
–100	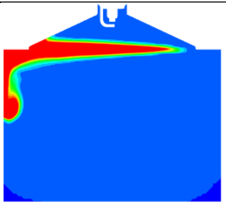	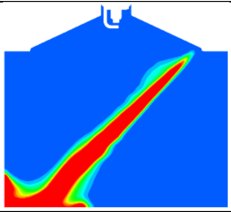	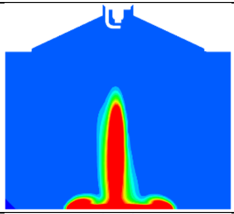	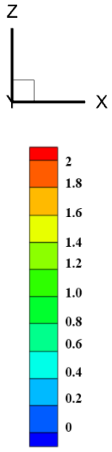
–80	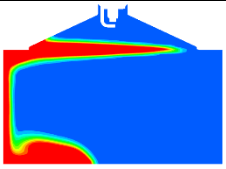	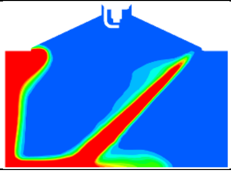	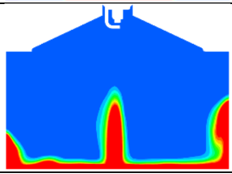	
–70	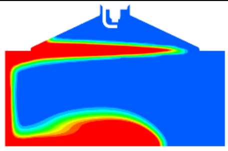	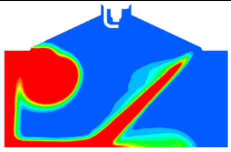	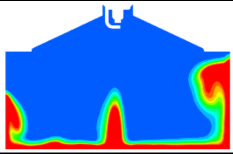	
–60	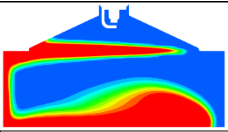	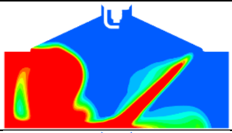	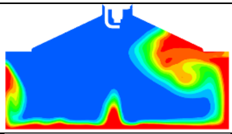	
–50	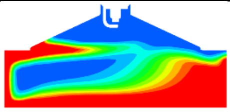	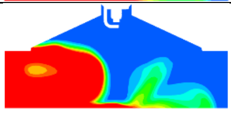	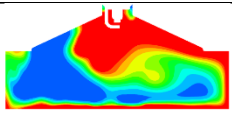	
–40	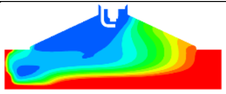	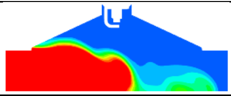	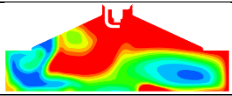	
–30	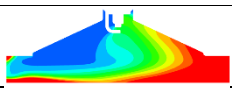	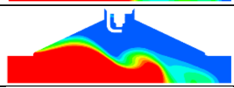	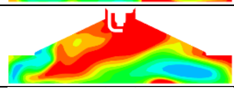	
–20	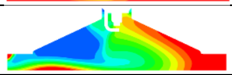	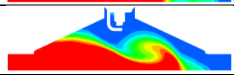	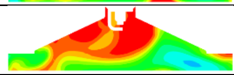	
–10	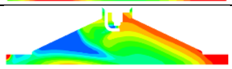	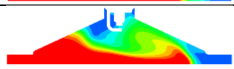	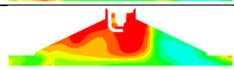	
–5	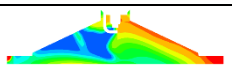	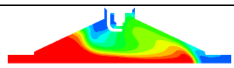	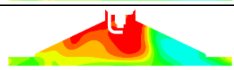	
0	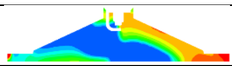	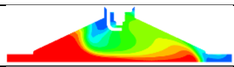	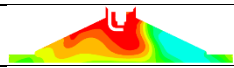	
5	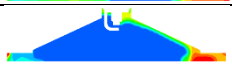	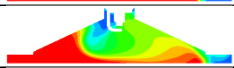	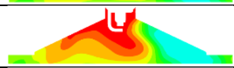	
10		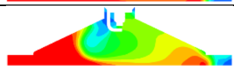	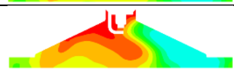	

3.6. In-cylinder pressure development

Figure 10 presents the variation of in-cylinder pressure with crank angle for all nine injection strategies. The pressure traces reflect not only the timing of ignition and flame propagation but also the degree of mixture uniformity and completeness of combustion.

The results show that mIVL injections – specifically WG-I@mIVL and AG-I@mIVL – produce the most favorable pressure development. Both strategies exhibit early, steep pressure rises, culminating in high peak pressures indicative of rapid, complete combustion. WG-I@mIVL delivers the sharpest and highest peak, confirming its superior mixture preparation and kernel development. The wall guidance redirects the spray, ensuring stoichiometric conditions near the spark and reducing wall-film persistence, resulting in efficient burn phasing.

In contrast, aIVO strategies show a more gradual pressure rise. Although early injection allows long residence time (around 58.3 ms), excessive interaction with walls and valve flows reduces local charge stratification near the spark. This leads to slower flame propagation, manifesting as smoother but delayed pressure development.

The aIVC injections present the most unfavorable pressure evolution. SG-I@aIVC demonstrates significantly delayed and reduced pressure peaks, symptomatic of incomplete combustion. Limited mixing time (about 17.5 ms) and reduced turbulence prevent thorough vapor–air interaction, leading to persistent, localized rich pockets. Even though bulk gas temperatures are higher at injection onset, the restricted transport window undermines overall combustion quality.

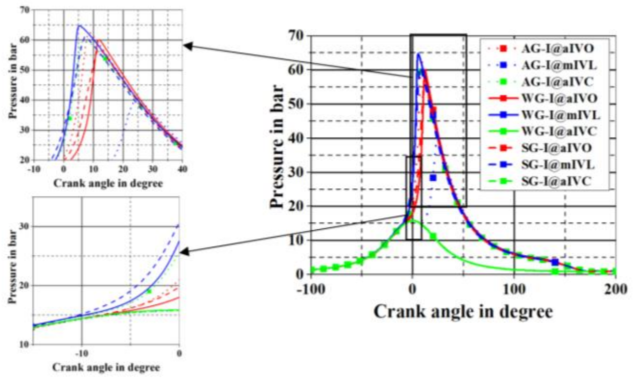

Fig. 10. Temporal variation of in-cylinder pressure

3.7. In-cylinder temperature evolution

Figure 11 illustrates the temporal evolution of in-cylinder temperature for the nine cases. Temperature rise is strongly correlated with heat release rate and, indirectly, with pressure development.

The data show that WG-I@mIVL achieves the highest peak temperatures, followed closely by AG-I@mIVL. Elevated temperatures persist throughout the expansion stroke, confirming that energy release was both rapid and well-phased with piston motion. This sustained thermal profile translates into superior indicated work and efficiency.

The aIVO cases exhibit intermediate peak temperatures. Early mixing produces a relatively homogeneous charge, but the broad distribution of droplets and potential wall cooling effects dampen thermal intensity. Still, combustion remains efficient, and post-ignition temperatures remain moderate.

The aIVC strategies display the lowest peak temperatures. SG-I@aIVC struggles to achieve high values due to poor ignition and delayed combustion. While residual fuel-rich regions eventually burn, they do so late in the cycle, when expansion has already reduced the potential pressure and temperature. As a result, both peak temperatures and post-combustion thermal retention are diminished.

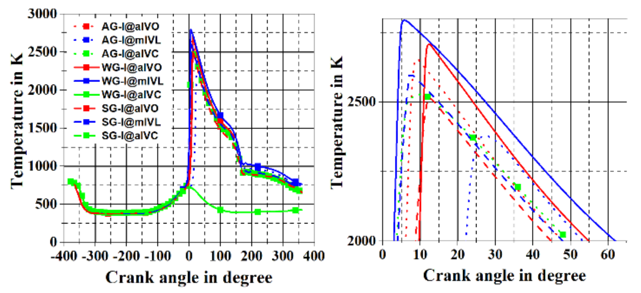

Fig. 11. Temporal variation of temperature

3.8. Heat release rate

Figure 12 shows the temporal heat release rate, which provides direct insight into combustion intensity and phasing. Among all cases, WG-I@mIVL exhibits the sharpest and highest HRR peak, corresponding to rapid combustion immediately following spark discharge. The narrow and well-centered HRR curve indicates compact combustion phasing, maximizing thermal-to-mechanical energy conversion.

AG-I@mIVL also delivers strong HRR, although the peak is slightly lower and broader than that of WG-I @mIVL. This suggests good, but less consistent, stratification near the spark, resulting in a marginally longer burn duration.

The aIVO strategies produce lower, more distributed HRR peaks. Their extended premixing time ensures homogeneous combustion, but at the cost of longer burn duration and reduced phasing efficiency.

By contrast, the aIVC cases exhibit weak, delayed HRR curves. The lowest amplitude and longest duration are seen in SG-I@aIVC, confirming its inferior mixture preparation and incomplete oxidation. These characteristics align with its pressure and temperature deficits (Fig. 10 and Fig. 11).

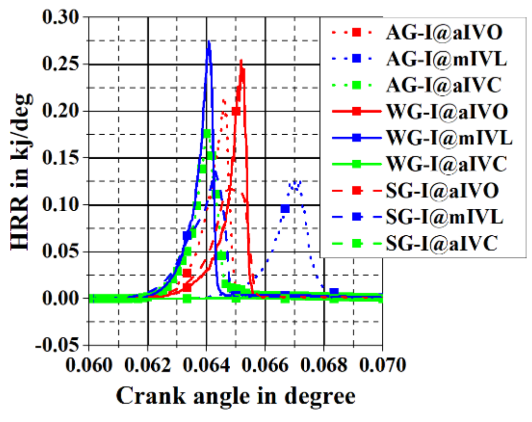

Fig. 12. Temporal variation of heat release rate

3.9. Spatial temperature distributions

Tables 9–11 illustrate temporal temperature fields for aIVO, mIVL, and aIVC strategies, respectively. The distributions highlight how injection timing and guidance influence flame spread and thermal uniformity.

For aIVO (Table 9), temperature fields are relatively broad but less intense, reflecting distributed combustion from a largely homogeneous charge. Local hot spots are minimized, but overall peak temperatures remain moderate.

In mIVL cases (Table 10), temperature distributions are more concentrated and elevated. WG-I@mIVL shows uniformly high thermal regions across the chamber, indicating efficient combustion propagation. This uniformity is especially important for reducing incomplete combustion. SG-I @mIVL, while delivering higher temperatures than aIVO, exhibits localized zones of elevated heat, signaling less efficient mixture distribution.

The aIVC strategies (Table 11) produce uneven temperature fields. Rich pockets ignite late, forming localized high-temperature spots surrounded by colder regions. This heterogeneity contributes to elevated unburned hydrocarbons (UHCs) and carbon monoxide (CO), as well as increased risk of knock if localized pressures spike.

Table 9. Temporal temperature distribution at SOI after inlet valve opening

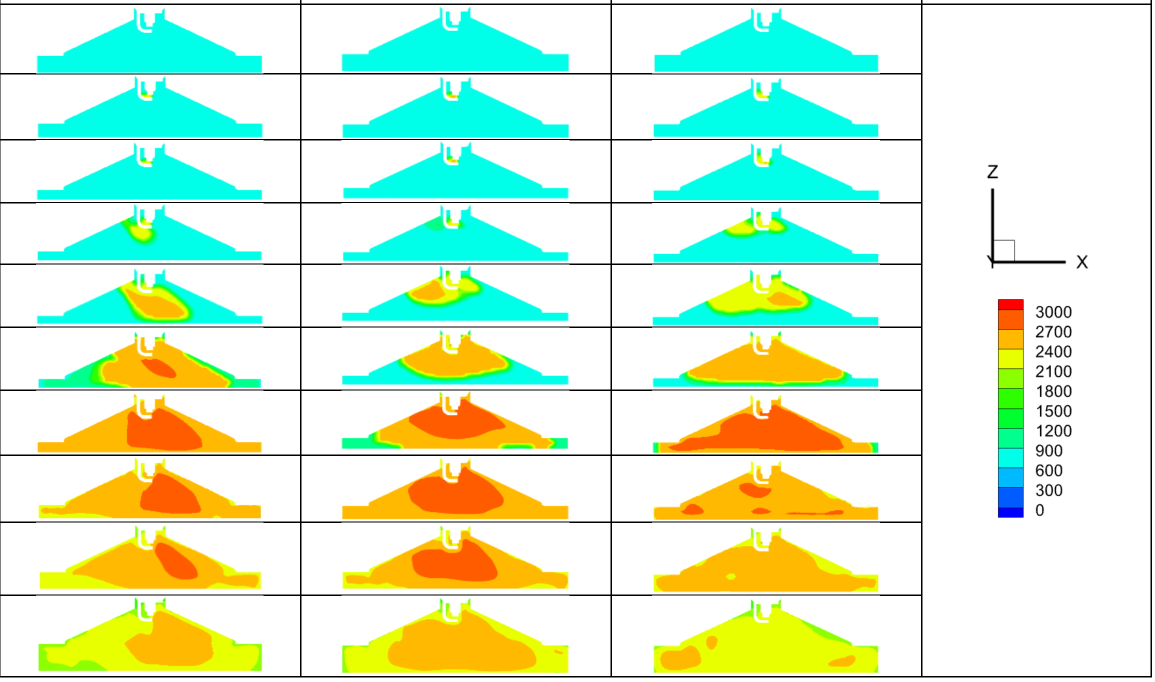

Crank angle [°CA]	Air guide fuel injection	Wall guide fuel injection	Spray guide fuel injection	Direction and color indices
-20				
-15				
-10				
-5				
0				
5				
10				
15				
20				
30				

Table 10. Temporal temperature distribution at SOI after maximum inlet valve lift

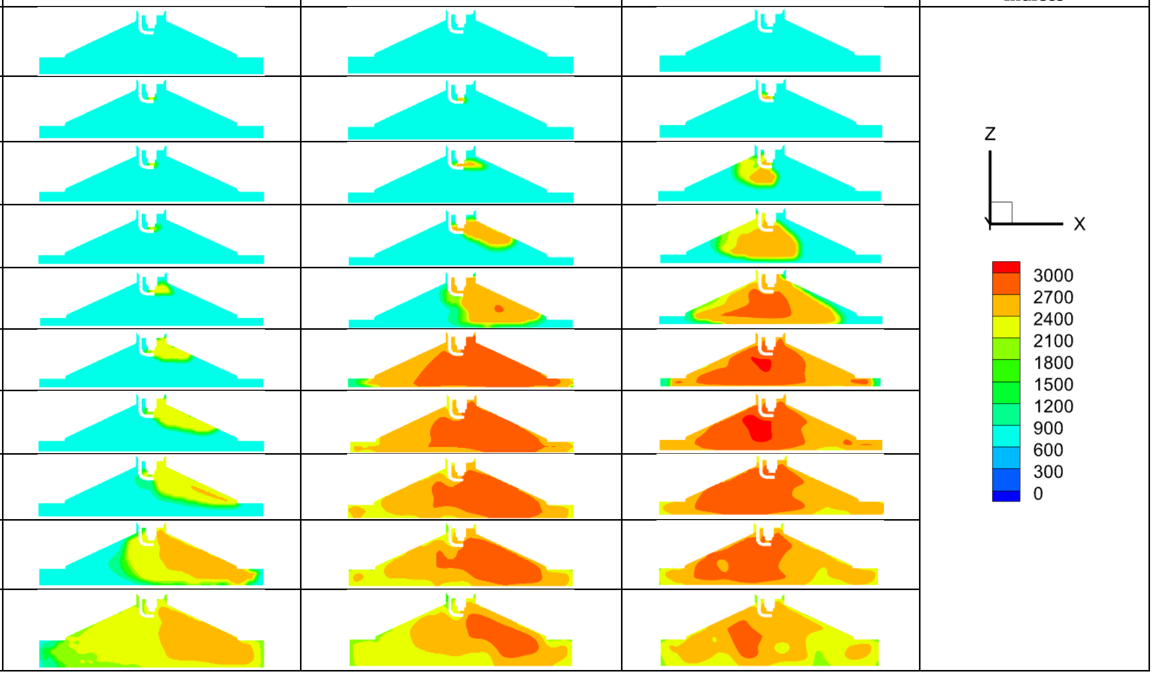

Crank angle [°CA]	Air guide fuel injection	Wall guide fuel injection	Spray guide fuel injection	Direction and color indices
-20				
-15				
-10				
-5				
0				
5				
10				
15				
20				
30				

3.10. Carbon monoxide emissions

Figure 13 presents CO emissions. The lowest CO levels are achieved with WG-I@mIVL, consistent with its high combustion completeness and favorable HRR profile. AG-I @mIVL also performs well, though slightly higher CO levels reflect less effective stratification.

The aIVO strategies achieve intermediate CO levels. Their broader combustion event consumes most of the fuel but leaves small amounts of residual CO due to extended flame quenching near walls.

aIVC injections yield the highest CO emissions, particularly SG-I@aIVC, which demonstrates substantial incomplete oxidation. The lack of time for vapor dispersion results in over-rich zones that burn inefficiently, producing carbon monoxide as the dominant by-product.

Table 11. Temporal temperature distribution at SOI after inlet valve closing

Crank angle in degree	Air Guide Fuel Injection	Wall Guide Fuel Injection	Spray Guide Fuel Injection	Direction and Color Indices
-20				
-15				
-10				
-5				
0				
5				
10				
15				
20				
30				

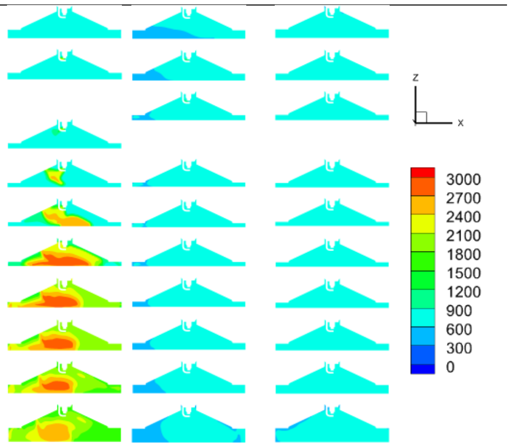

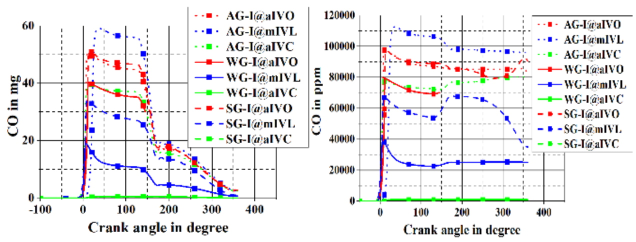

Fig. 13. Temporal variation of carbon monoxide

3.11. Nitrogen oxide (NO_x) emissions

The NO_x emissions, depicted in Fig. 14, are governed primarily by temperature and residence time at high temperatures. WG-I@mIVL and AG-I@mIVL produce the highest peak temperatures (Fig. 11), suggesting strong NO formation potential. However, because these cases feature compact HRR and earlier combustion phasing, the residence time at elevated temperature is relatively short. As a result, integrated NO_x levels remain moderate.

In contrast, SG-I@aIVC exhibits significant NO_x emissions despite lower global temperatures. This arises from localized hot spots in stratified zones, where pockets of near-stoichiometric vapor undergo extended burning. These conditions sustain high local thermal loads, promoting NO_x even as bulk combustion quality is poor.

The aIVO cases show relatively balanced NO_x output. Early premixing distributes heat release across the chamber, preventing excessive local temperatures while sustaining high-temperature residence times, thereby producing moderate levels of NO_x.

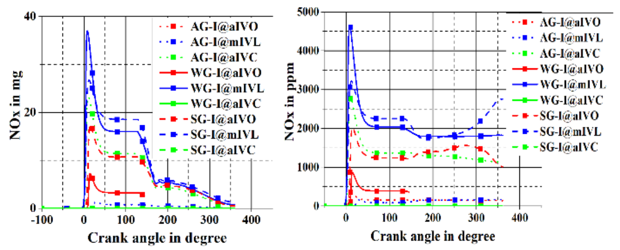

Fig. 14. Temporal variation of nitrogen oxides

3.12. Unburned hydrocarbons (HC)

The temporal evolution of unburned hydrocarbon emissions is shown in Fig. 15. These results are a sensitive indicator of mixture preparation, flame propagation efficiency, and quenching effects.

The WG-I@mIVL configuration achieves the lowest HC levels among all cases. Its superior mixture uniformity (Table 7) and concentrated temperature field (Table 10) minimize wall quenching and residual fuel pockets, enabling near-complete oxidation. AG-I@mIVL follows closely, producing slightly higher HC emissions due to less consistent guidance of the spray plume, which occasionally allows minor regions of poor fuel–air interaction.

The aIVO cases show moderate HC emissions. Although long residence time facilitates vaporization, the extended distribution of liquid fuel increases the probability of wall films forming in piston crevices and near the cylinder liner. These films evaporate late or not at all, contributing to higher HC emissions.

The highest HC levels are found in aIVC strategies, with SG-I@aIVC being the most unfavorable. Limited premixing time (~17.5 ms before spark) leaves substantial fuel-rich zones that burn incompletely. This localized combustion results in poor flame penetration and persistent hydrocarbons in the exhaust stream.

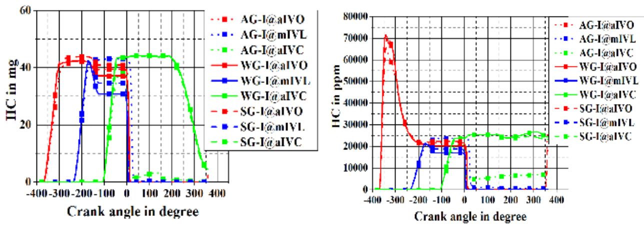

Fig. 15. Temporal variation of unburnt hydrocarbon

3.13. Carbon dioxide

Figure 16 illustrates CO_2 emissions, which serve as a direct measure of combustion completeness. The WG-I @mIVL strategy yields the highest CO_2 concentrations, confirming its superior oxidation efficiency and energy release. Elevated CO_2 levels indicate that nearly all carbon atoms in the fuel were fully oxidized.

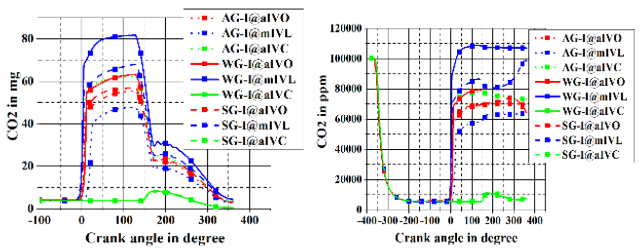

Fig. 16. Temporal variation of carbon dioxide

AG-I@mIVL also shows strong CO_2 emissions, albeit marginally lower than wall guidance. The slight reduction corresponds to small inefficiencies in stratification and localized incomplete combustion.

In contrast, aIVO cases produce moderate CO_2, reflecting the balance between broad vapor dispersion and wall-film quenching. Although the overall combustion is relatively complete, not all injected fuel is fully oxidized.

The lowest CO_2 emissions occur with aIVC strategies, particularly SG-I@aIVC, which produces weak and segmented combustion (Fig. 12). Here, a significant fraction of fuel carbon remains in partially oxidized species such as CO and UHC, resulting in reduced CO_2 yield.

3.14. Synthesis of combustion-emission trade-offs

The combined analysis of Fig. 5–16 and Tables 6–11 demonstrates the decisive influence of synchronizing injector guidance with start-of-injection (SOI) timing. Among the nine configurations examined, Wall-Guided Injection at Maximum Inlet Valve Lift (WG-I@mIVL) consistently achieved the most favorable balance of combustion and emission performance. This strategy produced the highest in-cylinder pressure (Fig. 10) and temperature (Fig. 11), coupled with the sharpest and most compact heat release rate (HRR) peak (Fig. 12). Furthermore, it yielded a uniform thermal distribution (Table 10), minimized carbon monoxide (CO, Fig. 13) and unburned hydrocarbon (HC, Fig. 15) formation, and generated the highest carbon dioxide (CO_2, Fig. 16), which is a direct indicator of complete oxidation. Although nitrogen oxides (NO_x, Fig. 14) were present due to elevated peak temperatures, their formation was moderated by the compact burn duration characteristic of this strategy.

Air-guided injection at mIVL (AG-I@mIVL) also displayed robust performance, with turbulence-driven entrainment supporting effective fuel–air interaction and oxidation. The observed sensitivity of combustion outcomes to the alignment of SOI with intake-driven flow structures is consistent with the broader GDI literature emphasizing injection phasing as a primary lever for mixture preparation and combustion stability [3, 7, 12]. However, many prior studies evaluate SOI effects without simultaneously varying injector targeting philosophy, or they report guidance effects under a fixed SOI schedule. The present results show that the effectiveness of any guidance concept depends on whether injection occurs during a high-tumble/high-entrainment window (mIVL) or during the decay of intake-generated motion (aIVC). This coupling explains why the wall-guided strategy – although historically established – remains advantageous under certain phasing conditions: piston-surface redirection enhances breakup and entrainment when the surrounding flow field can transport and homogenise the resulting droplet fragments. Conversely, late SOI reduces the utility of guidance because the flow field lacks sufficient kinetic energy to distribute vapour and suppress locally rich pockets, leading to incomplete oxidation and elevated CO/UHC, consistent with injection-pattern and spray-development sensitivities reported in injector dynamics studies [21, 22, 25, 26]. In this sense, the study advances current understanding by quantifying the combined SOI–guidance dependency under controlled conditions, thereby providing calibration-relevant evidence for synchronizing injector targeting with valve-event-driven flow evolution.

In contrast, late injection strategies (aIVC) were fundamentally disadvantaged. With only ~17.5 ms of premixing time available before ignition and significantly reduced turbulence intensity, these cases consistently delivered low pressure, reduced peak temperatures, and weak HRR profiles. The mixture quality was poor, resulting in incomplete combustion and elevated CO and HC emissions. Among these, Spray-Guided Injection at aIVC (SG-I@aIVC) emerged as the least favorable, with incomplete combustion, localized hot spots, and markedly poor overall efficiency. Collectively, these observations confirm that the most effective combustion in GDI engines requires the synchronization of injector guidance with valve dynamics, with wall-guided injection at peak intake lift providing the optimal combination of mixture preparation, phasing, and emissions control.

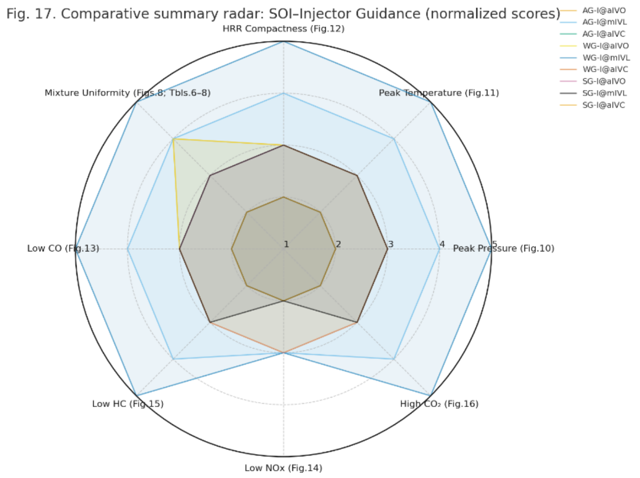

Fig. 17. Comparative summary

3.15. Practical implications

The present findings are consistent with previous studies showing that earlier injection generally improves evaporation and mixture homogeneity by increasing the available mixing time before ignition. Recent direct-injection spark-ignition simulations using n-butanol reported that injection timing strongly affects in-cylinder flow, mixture formation, combustion quality, and emissions, with longer mixing duration improving charge preparation but influencing nitrogen oxide formation through temperature changes. The present results support this general trend because the aIVO cases provide extended premixing and moderate combustion behaviour, whereas aIVC cases suffer from insufficient residence time, poor vapour distribution, and elevated incomplete-combustion products.

However, the present work also shows that longer mixing time alone does not guarantee optimum combustion. The best case was obtained when injection occurred at maximum intake valve lift, where intake-driven turbulence was strongest and the spray could be entrained into an energetic tumble field. This explains why the mIVL cases, particularly wall-guided injection at mIVL, produced stronger pressure development, more compact heat release, and lower carbon monoxide and hydrocarbon formation than the late-injection cases. The result extends earlier SOI-focused studies by showing that the benefit of injection timing depends strongly on the guidance strategy and the instantaneous flow structure inside the cylinder.

The findings also agree with recent injector-focused GDI studies showing that injector configuration and spray targeting modify combustion and emissions by altering stratification, wall interaction, and fuel–air preparation. In the present case, spray-guided injection was less effective at late timing because the plume remained locally concentrated and had insufficient time to mix before spark ignition. This behaviour is consistent with injector-zone and wall-film studies that identify fuel-rich liquid or vapour regions as important contributors to incomplete combustion and particulate-related emission pathways.

Therefore, the present study advances the current understanding by demonstrating that SOI and injector guidance should not be treated as independent calibration variables. The main contribution is the identification of a coupled optimum: wall-guided injection becomes most effective when piston-crown redirection is synchronised with maximum intake-valve-induced turbulence, while the same guidance concept becomes less beneficial when the surrounding flow field has decayed. This explains the superior performance of wall-guided injection at maximum intake valve lift and the poor performance of spray-guided injection after intake valve closing.

3.16. Limitations and scope for future work

Although the present simulations provided comprehensive insights, several limitations must be acknowledged. All cases were performed under controlled baseline conditions, with fixed injection pressure (50 bar), injected mass (4.398×10^{-5} kg), spark timing (−20° crank angle bTDC), and global equivalence ratio ($\phi = 1.2$). These constraints effectively isolated the roles of SOI and injector guidance; however, real-world engines operate across wider regimes that include variable fueling, multipulse injection strategies, transient thermal boundary conditions, and higher rotational speeds. Future extensions should therefore evaluate multi-cycle variability and engine load transitions to establish broader applicability.

Additionally, soot modeling was omitted because the present study focused on lean operation where particulate formation is minimal. Extending simulations to stratified-rich modes would allow a deeper understanding of particulate matter formation mechanisms and their trade-offs with NO_x reduction. Injector design variations – including nozzle hole count, distribution, and spray cone angle – should also be investigated, as these parameters can influence fuel breakup and chamber interaction. Furthermore, piston crown geometries optimized for spray deflection could amplify the benefits of wall-guided strategies. Finally, coupling the computational results with experimental optical diagnostics, such as high-speed imaging of spray–air interaction and flame kernel development, would provide essential validation and enhance confidence in the model fidelity.

3.17. Concluding remarks on results

The systematic evaluation of nine GDI injection strategies confirms that wall-guided injection at maximum intake valve lift (WG-I@mIVL) offers the best balance between efficiency and emissions. This configuration ensured strong tumble-driven entrainment, a near-stoichiometric equivalence ratio at the spark plug, compact and efficient heat release, and elevated in-cylinder pressure and temperature, all of which supported superior oxidation efficiency. The emission trends corroborated this advantage, with WG-I @mIVL achieving high CO_2 output accompanied by minimal CO and HC formation.

Air-guided injection at mIVL offered comparable performance, particularly in terms of turbulence-driven mixing, but greater variability limited its robustness. Conversely, spray-guided injection at late timings consistently underperformed, delivering poor mixture stratification, delayed combustion, and excessive pollutant formation. The overarching conclusion is that injector guidance and SOI timing must be tuned jointly rather than considered independently. Their coupled effects determine mixture preparation, flame propagation, and pollutant formation, making them critical levers in the pursuit of precision combustion strategies for next-generation gasoline direct-injection engines.

4. Conclusions

This study has examined the coupled influence of injector guidance strategies and start-of-injection (SOI) timing on mixture preparation, combustion phasing, and emissions in a gasoline direct injection (GDI) engine using a validated CFD framework. Nine distinct configurations were investigated, encompassing air-guided, wall-guided, and spray-guided injection orientations at three SOI timings: after inlet valve opening (aIVO), maximum inlet valve lift (mIVL), and after inlet valve closing (aIVC). The results consistently revealed that optimal combustion is governed not by either parameter in isolation but by their combined effect on spray–air interaction and charge stratification.

Among the strategies evaluated, Wall-Guided Injection at Maximum Inlet Valve Lift (WG-I@mIVL) emerged as the most effective configuration. This approach exploited piston crown geometry to redirect spray momentum toward the chamber center while leveraging maximum intake-induced turbulence. As a result, WG-I@mIVL achieved the highest in-cylinder pressure and temperature, the sharpest and most compact heat release rate, and a uniformly distributed thermal field. These characteristics promoted rapid ignition and stable flame propagation. In terms of emissions, this strategy minimized carbon monoxide and unburned hydrocarbons, elevated carbon dioxide output indicative of efficient oxidation, and moderated nitrogen oxide formation despite high peak temperatures, owing to the short burn duration. Collectively, WG-I@mIVL balanced mixture homogeneity with local stratification in a manner that optimized both efficiency and environmental performance.

Air-guided injection at mIVL also demonstrated strong performance. The turbulence-driven entrainment produced efficient oxidation and competitive pressure–temperature development. However, its reliance on airflow rather than geometric guidance introduced greater cycle-to-cycle variability. Early injection strategies (aIVO) benefited from extended premixing intervals, approximately 58.3 ms at 1000 rpm, leading to relatively homogeneous charges and distributed temperature fields. This reduced NO_x formation but increased wall-film deposition risks and prolonged combustion, which elevated CO and HC emissions compared to WG-I@mIVL.

Late injection cases (aIVC) were consistently disadvantaged. With only ~17.5 ms of premixing time and weakened turbulence, these strategies produced lower pressure and temperature, weak heat release rates, and poor mixture quality. Incomplete combustion followed, resulting in high CO and HC emissions. Spray-Guided Injection at aIVC performed worst, combining localized hot spots with high pollutant levels and overall reduced efficiency. These observations demonstrate that injection strategies aligned with valve dynamics are critical; when spray and airflow synergies are absent, combustion quality deteriorates substantially.

The synthesis of results underscores three key mechanistic insights. First, mixture uniformity and stratification are dictated by the interaction of injection timing with intake-driven tumble. Mid-phase injection maximizes turbulence utilization, whereas late injection suppresses it. Second, geometric redirection through wall guidance provides a reliable means of steering the spray without excessive wall impingement, contrary to common concerns. Third, pollutant formation is strongly correlated with combustion phasing: compact heat release limits NO_x despite high peak temperatures, while complete oxidation minimizes CO and HC.

From a practical standpoint, these findings have implications for injector design and control calibration. Injector orientation must be optimized with piston crown geometry to guide the spray effectively, and SOI should coincide with maximum valve lift to ensure residence times on the order of ~35 ms before spark. Although WG-I@mIVL increases thermal loads that may elevate NO_x under high-load conditions, mitigation strategies such as cooled exhaust gas recirculation or minor spark retardation can alleviate this without eroding efficiency. Conversely, late-injection modes are unsuitable for homogeneous operation and may be relevant only in specialized stratified-charge regimes that require alternative chamber geometries.

The present analysis, while comprehensive, was conducted under controlled baseline conditions with fixed injection pressure (50 bar), injected mass (4.398×10^{-5} kg), spark timing (20°CA bTDC), and equivalence ratio (ϕ = 1.2). These constraints isolated the effects of SOI and injector guidance but did not address transient load variation, multipulse injection, or higher engine speeds. Moreover, soot modeling was excluded under lean operation. Future studies should extend this framework to stratified-rich conditions, explore variations in injector design, and couple CFD predictions with optical diagnostics to directly capture spray–air and flame interactions.

Ultimately, the investigation confirms that the synergy of injector guidance and SOI timing is the principal determinant of combustion efficiency and emission control in GDI engines. Wall-Guided Injection at Maximum Inlet Valve Lift provides the most favorable balance of pressure, temperature, heat release, and pollutant suppression. The results emphasize that injector orientation and timing must be optimized jointly rather than independently. This insight provides a foundation for precision combustion strategies aimed at achieving both high efficiency and compliance with increasingly stringent emission regulations, reinforcing the relevance of GDI technology in next-generation spark-ignition powertrains.

Acknowledgements

The authors express their gratitude to the Department of Mechanical Engineering, Annamalai University, for providing the computational facilities and technical resources essential to the completion of this work. Special acknowledgment is extended to faculty mentors and colleagues for their constructive guidance during the study. The authors also appreciate the institutional support in accessing licensed computational fluid dynamics (CFD) tools, without which the high-fidelity simulations would not have been possible.

In addition, the authors acknowledge the valuable insights from prior literature that served as the basis for model validation and benchmarking. Support from laboratory staff in maintaining computational hardware and providing operational assistance is also recognized. Any funding sources, fellowships, or research grants that contributed to this investigation should be formally acknowledged here in accordance with the requirements of the target journal.

Bibliography

[1] Bui VG, Bui TMT, Nguyen MT, Bui VH, Do PN, Tran NAH et al. Enhancing the performance of syngas-diesel dual-fuel engines by optimizing injection regimes: from comparative analysis to control strategy proposal. Process Saf Environ Prot. 2024;186:1034-1052. https://doi.org/10.1016/j.psep.2024.04.042

[2] Gaur A, Saha K, Ghai D. Experimental analysis of the near-nozzle direct injection spray for gasoline and ethanol-gasoline blended fuels. Exp Therm Fluid Sci. 2024;153: 111142. https://doi.org/10.1016/j.expthermflusci.2024.111142

[3] Ji C, Cong X, Wang S, Shi L, Su T, Du W. Performance of a hydrogen-blended gasoline direct injection engine under various second gasoline direct injection timings. Energy Convers Manage. 2018;171:1704-1711. https://doi.org/10.1016/j.enconman.2018.06.112

[4] Kumar MS, Muniyappan M. Experimental and CFD analysis of the influence of fuel injection timing on the behavior of a gasohol-based GDI engine. Energy Sources Part A Recovery Util Environ Eff. 2024;46(1):2448-2460. https://doi.org/10.1080/15567036.2024.2307365

[5] Li A, Zheng Z, Peng T. Effect of water injection on the knock, combustion, and emissions of a direct injection gasoline engine. Fuel. 2020;268:117376. https://doi.org/10.1016/j.fuel.2020.117376

[6] Liu Q, Wang C, Hu Y, Chen H. Flatness-based feedforward and feedback control for fuel rail system of gasoline direct injection engine. IFAC-PapersOnLine. 2016;49(11):775-780. https://doi.org/10.1016/j.ifacol.2016.08.113

[7] Liu ZB, Zhen XD, Geng J, Tian Z. Effects of injection timing on mixture formation, combustion, and emission characteristics in an n-butanol direct injection spark ignition engine. Energy. 2024;295:131059. https://doi.org/10.1016/j.energy.2024.131059

[8] Macian V, Payri R, Ruiz S, Bardi M, Plazas AH. Experimental study of the relationship between injection rate shape

and diesel ignition using a novel piezo-actuated direct-acting injector. Appl Energy. 2014;118:100-113. https://doi.org/10.1016/j.apenergy.2013.12.025

[9] Payri R, Bracho G, Gimeno J, Bautista A. Rate of injection modelling for gasoline direct injectors. Energy Convers Manage. 2018;166:424-432. https://doi.org/10.1016/j.enconman.2018.04.041

[10] Pielecha I. Fuel injection rate shaping and its effect on spray parameters in a direct-injection gasoline system. J Vis. 2022; 25;727-740. https://doi.org/10.1007/s12650-021-00823-6

[11] Ramesh P, Gunasekaran EJ. Numerical simulation of film thickness formation in a PFI engine under motoring conditions. Bonfring Int J Ind Eng Manage Sci. 2019;9(3):11-15. https://doi.org/10.9756/BIJIEMS.9032

[12] Shuai S, Ma X, Li Y, Qi Y, Xu H. Recent progress in automotive gasoline direct injection engine technology. Automot Innov. 2018;1(2):95-113. https://doi.org/10.1007/s42154-018-0020-1

[13] Tian J, Wang L, Xiong Y, Wang Y, Yin W, Tian G et al. Enhancing combustion efficiency and reducing nitrogen oxide emissions from ammonia combustion: a comprehensive review. Process Saf Environ Prot. 2024;183:514-543. https://doi.org/10.1016/j.psep.2024.01.020

[14] Tian J, Xiong Y, Liu Z, Wang L, Wang Y, Yin W et al. Experimental study on the discharge characteristics of high-voltage nanosecond pulsed discharges and its effect on the ignition and combustion processes. Appl Energy. 2024;374: 124011. https://doi.org/10.1016/j.apenergy.2024.124011

[15] Tian J, Xiong Y, Wang L, Wang Y, Liu P, Shi X et al. Experimental study of the effect of nanosecond pulse discharge parameters on the methane-air mixture combustion. Fuel. 2024;364:131166. https://doi.org/10.1016/j.fuel.2024.131166

[16] Vasan V, Sridharan NV, Feroskhan M, Vaithiyanathan S, Subramanian B, Tsai P-C et al. Biogas production and its utilization in internal combustion engines – a review. Process Saf Environ Prot. 2024;186:518-539. https://doi.org/10.1016/j.psep.2024.04.014.

[17] Wang L, Gao K, Han J, Zhao X, Liu L, Pan C et al. Battery pack SOC estimation by noise matrix self-adjustment-extended Kalman filter algorithm based on cloud data. J Energy Storage. 2024;84:110706. https://doi.org/10.1016/j.est.2024.110706

[18] Wang X, Zhao H, Xie H. Effect of dilution strategies and direct injection ratios on stratified flame ignition (SFI) hybrid combustion in a PFI/DI gasoline engine. Appl Energy. 2016;165:801-814. https://doi.org/10.1016/j.apenergy.2015.12.116

[19] Wang X, Zhao H, Xie H, He B-Q. Numerical study of the effect of piston shapes and fuel injection strategies on in-cylinder conditions in a PFI/GDI gasoline engine. SAE Int J Engines. 2014;7(4):1888-1899. https://doi.org/10.4271/2014-01-2670

[20] Wang Y, Cai H, Hu X, Liu P, Yan Q, Cheng Y. Data-driven method for estimating emission factors of multiple pollutants from excavators based on portable emission measurement system and online driving characteristic identification. Sci Total Environ. 2023;912:169472. https://doi.org/10.1016/j.scitotenv.2023.169472

[21] Wang Y, Cheng Y, Xiong Y, Yan Q. Estimation of battery open-circuit voltage and state of charge based on dynamic matrix control-extended Kalman filter algorithm. J Energy Storage. 2022;52:104860. https://doi.org/10.1016/j.est.2022.104860

[22] Wang Y, Hu X, Deng X, Cheng Y, Yin W. Design and experiment of a low-temperature charging preheating system for power battery packs with an integrated dissipative balancing function. J Power Sources. 2023;588:233740. https://doi.org/10.1016/j.jpowsour.2023.233740

[23] Xiong Q, Zhang Y, Wang D, Zhang X, Liu Y, Ding X. Optimization design of a common rail injector based on NSGA-II algorithm. Trans Beijing Inst Technol. 2010; 30(10):1160-1164.

[24] Zhang M, Ju Y, Song R, Wang D, Wang Z. Influence of driving parameters on GDI piezoelectric injector. Vehicle Engine. 2016;4:51-55.

[25] Zhang Z, Liu H, Li Y, Ye Y, Tian J, Li J et al. Research and optimization of hydrogen addition and EGR on the combustion, performance, and emission of the biodiesel-hydrogen dual-fuel engine with different loads based on the RSM. Heliyon. 2024;10(1):e23389. https://doi.org/10.1016/j.heliyon.2023.e23389

[26] Zhao X, Wang L, Zhou Y, Pan B, Wang R, Wang L et al. Energy management strategies for fuel cell hybrid electric vehicles: classification, comparison, and outlook. Energy Convers Manage. 2022;270:116179. https://doi.org/10.1016/j.enconman.2022.116179

[27] Zhen X, Tian Z, Wang Y, Liu D, Li X. A model to determine the effects of low proportion of hydrogen and the flame kernel radius on combustion and emission performance of direct injection spark ignition engine. Process Saf Environ Prot. 2021;147:1110-1124. https://doi.org/10.1016/j.psep.2021.01.040

Madireddi Ananda Kumar – Department of Mechanical Engineering, Annamalai University, Annamalainagar, Chidambaram, Tamil Nadu 608002, India.
e-mail: *anandkumar.madireddy@gmail.com*

Prof. Perumal Ramesh – Department of Mechanical Engineering, Annamalai University, Annamalainagar, Chidambaram, Tamil Nadu 608002, India.
e-mail: *erprlme_2000@yahoo.co.in*

Prof. Edward James Gunasekaran – Department of Mechanical Engineering, Annamalai University, Annamalainagar, Chidambaram, Tamil Nadu 608002, India.
e-mail: *jamesgunasekaran@gmail.com*

Mahendiran Karthikeyan – Department of Mechanical Engineering, Annamalai University, Annamalainagar, Chidambaram, Tamil Nadu 608002, India.
e-mail: *kanchikarthi2010@gmail.com*